Soft Matter

REVIEW

View Article Online
View Journal

Cite this: DOI: 10.1039/d5sm01134e

Liquid–liquid phase separation as a structuring tool for designing anisotropic food systems

Ashkan Madadlou

Received 12th November 2025,
Accepted 6th March 2026

DOI: 10.1039/d5sm01134e

rsc.li/soft-matter-journal

Liquid–liquid phase separation (LLPS) is a key mechanism in the formation of biomolecular condensates in cells and provides a versatile framework for structuring soft materials. In food systems, LLPS spans applications from droplet-based compartmentalisation (*e.g.*, microencapsulation by complex coacervates and droplet microreactors) to flow-induced alignment strategies that generate anisotropic textures. This review examines the associative LLPS (coacervate dispersions), and segregative LPPS (aqueous two-phase systems) through the lens of deformation, relaxation and arrest. For coacervates, bulk viscosity is interpreted using deformable-droplet rheology. I then summarise the state of the art in coacervate-derived hydrogel fabrication. For segregative systems, polymer– demixing coupled with shear and controlled arrest enables alignment, string formation, and phase inversion prior to solidification. Across scales from single droplets to bulk flow, physics-based descriptors such as capillary number Ca, viscosity ratio λ, and Weissenberg number Wi, are linked to image-derived orientation metrics to connect in-flow deformation and droplet arrest to the final structure. The analysis delineates governing mechanisms, processing windows, and limitations that define when LLPS yields an aligned microstructure and fibrous texture under practical conditions.

1. Introduction

Liquid-phase separation (LLPS) is a process in which a homogenous solution demixes into two coexisting liquid phases with distinct compositions. It is commonly classified as segregative and associative. Segregative LLPS arises from mutual exclusion/repulsion between unlike solutes (*e.g.*, two polymers), and yields two polymer-rich aqueous phases. The resulting system is an aqueous two-phase system (ATPS). Associative LLPS (coacervation) arises from favourable interactions between molecular species, which may be enthalpic (*e.g.*, electrostatic or hydrogen bonding) and/or entropic, including solvent-mediated effects such as counterion release and increased freedom of water molecules.[1] This results in a polymer-rich liquid phase coexisting with a polymer-poor phase. The dense phase often still contains >50 wt% solvent. Coacervation occurs as simple coacervation (a single polymer condenses upon desolvation by salt, antisolvent, pH or temperature change) or complex coacervation (two oppositely charged polymers associate to form the dense phase).[2–4] Fig. 1 schematically shows the internal structure of the droplets formed by complex coacervation and segregative LLPS (ATPS).

Phase diagrams (Fig. 2) for liquid–liquid demixing show single-phase and two-phase regions. The phase diagram in Fig. 2A, corresponds to simple coacervation, involving a single macromolecular component. The binodal is terminated by a critical point, at which the compositions of the dense and dilute phases become identical (*i.e.*, the dense phase is no longer denser in composition than the dilute phase). Under this condition, the phase boundary disappears, and the interfacial tension vanishes. Beyond this point, the mixture is thermodynamically single phase because there is no driving force for macroscopic demixing.[5] In segregative LLPS (Fig. 2B), two unlike polymers *X* and *Y* repel each other such that overall compositions lying inside the binodal split into an *X*-rich (light) phase and a *Y*-rich (dense) phase.

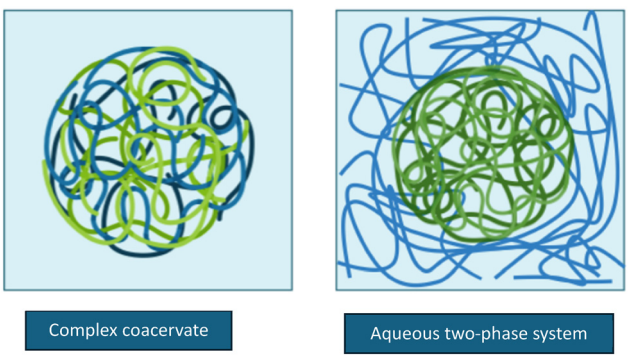

Fig. 1 Schematic representation of droplets formed by complex coacervation (associative LLPS) and aqueous two-phase systems (segregative LLPS).

School of Food and Nutritional Sciences, University College Cork, Cork, Ireland.
E-mail: Amadadlou@ucc.ie

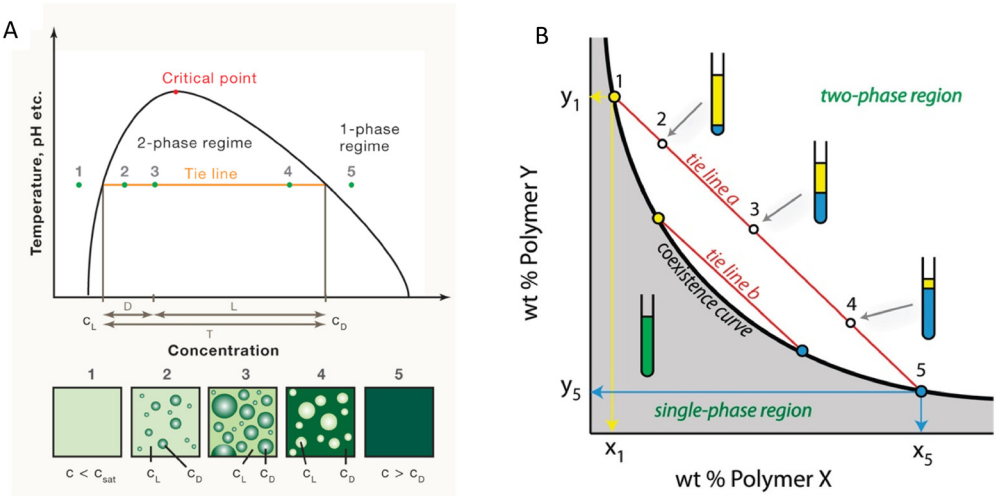

Fig. 2 Phase diagrams for liquid–liquid demixing. (A) Simple coacervation (one polymer): binodal with critical point; tie lines give the coexisting phase compositions, C_L (light phase) and C_D (dense phase). Along a tie line only phase amounts change, following the lever rule ($vf_L = L/T$, $vf_D = D/T$). (A) Adapted from ref. 5, *Cell*, 2019, **176**(3), 419–434. DOI: https://doi.org/10.1016/j.cell.2018.12.035, with permission from Elsevier, copyright 2019. (B) Segregative LLPS (two polymers): coexistence curve and tie lines. (B) Adapted from ref. 6, *Acc. Chem. Res.*, 2012, **45**(12), 2114–2124. DOI: https://doi.org/10.1021/ar200294y, with permission from American Chemical Society, copyright 2012.

Tie lines connect the coexisting compositions on the binodal. All overall compositions located on a given tie line (*e.g.*, points 2–4 in Fig. 2A) equilibrate to the same light- and dense-phase concentrations, C_L and C_D; only the relative phase amounts vary. Phase volume fractions follow the lever rule, and are proportional to the opposite arm of the tie line. If L and D denote the distances from the overall composition to the dense- and light-phase ends of the tie line, respectively, and $T = L + D$, then $vf_L = L/T$ and $vf_D = D/T$.[5,6]

It is important to distinguish coacervation from precipitation. Coacervation produces a condensed, macromolecule-rich liquid phase that separates from a more dilute continuous phase and commonly forms spherical droplets that flow, deform, and coalesce. Under small-amplitude oscillatory shear, many coacervate phases exhibit a predominantly viscous response over the measured frequency range, with the loss modulus G'' exceeding the storage modulus G'. For example, β-lactoglobulin–lactoferrin coacervates show $G'' \approx 100G'$[7] and whey protein–gum arabic coacervates show G'' up to about $\sim 10G'$.[8] Within such fluid coacervates, interaction partners exchange and polymer chains remain mobile across molecular-to-micron length scales and μs–s time scales, enabling translational diffusion and continual stress relaxation. By contrast, precipitates are typically dynamically arrested solids or aggregates in which strong attractions restrict partner exchange and diffusion.[9] Coacervate phases are not universally liquid only. Depending on the composition, concentration, temperature, ionic strength, crosslinking, and aging[10] coacervates span a broad mechanical spectrum, from low-viscosity liquids to strongly viscoelastic or gel-like materials, including systems that are dynamically arrested from the outset. In some associative systems, phase separation coincides with the formation of a percolated network within the dense phase, such that viscoelastic or arrested behaviour emerges already at demixing.[11–13]

For a broader discussion of LLPS in biological systems, including biomolecular condensates and membraneless organelles, readers are referred to dedicated reviews.[14–16] In cells, LLPS contributes to membraneless compartmentalisation in both the cytoplasm and the nucleus. Segregative LLPS (driven largely by poor compatibility) is illustrated by the multiphase nucleolus, where immiscible layers compartmentalise ribosomal RNA (rRNA) transcription, processing/modification, and assembly in adjacent yet compositionally distinct condensates.[17,18] In synthetic biology, LLPS is exploited to build artificial cells. For example, ATPS (water-in-water, W/W) emulsions formed by segregative phase separation of polyethylene glycol (PEG) and dextran (Dex) with liposomal particles at the W–W interface have been used as protocell bioreactors, enabling RNA enzyme compartmentalisation and a cleavage reaction.[19]

Analogous to cellular condensates and LLPS-based artificial cells/bioreactors, selective partitioning of biomolecules in ATPSs offers practical routes to control reactions in food ingredient technology. We recently used polymer–salt ATPSs to partition Maillard reaction precursors and drive the reaction either inside droplets or at the water–water interface. In the latter case, glucose and amino acids segregate into different phases yet meet and react at the liquid–liquid interface.[20] ATPSs built from natural deep eutectic solvent–salt pairs act as tunable pH microreactors that further steer the Maillard reaction pathway.[21]

2. LLPS in classic food science

A conventional application of LLPS in food science is microencapsulation. In complex coacervation, associative LLPS produces a polymer-rich liquid phase that can wet and coat dispersed cores such as edible oil droplets. Near charge stoichiometry, oppositely charged biopolymers form coacervate

droplets with ultralow coacervate–serum interfacial tension (Γ_{cs}), typically on the order of 1–100 μN m^{-1}.[22,23] The value of Γ_{cs} is strongly salt dependent and often decreases with increasing ionic strength until LLPS is eventually suppressed above a system-specific critical salt concentration.[24] Whether a coacervate spreads over an oil core can be rationalised using the spreading coefficient:

$$S_c = \Gamma_{so} - (\Gamma_{co} + \Gamma_{cs}) \quad (1)$$

where Γ_{so} is the serum–oil interfacial tension and Γ_{co} is the coacervate–oil interfacial tension. When $S_c > 0$ (*i.e.*, $\Gamma_{so} > \Gamma_{co} + \Gamma_{cs}$), the coacervate fully wets the oil and forms a liquid shell (core–shell). When $S_c < 0$ wetting is partial and the coacervate adopts a spherical-cap or "acorn" morphology with a finite contact angle. This transition and its correlation with microcapsule morphology and encapsulation efficiency were demonstrated for gelatin–gum arabic coacervate shells across oils of varying polarity.[25] Confocal imaging of gelatin-carboxymethyl cellulose (CMC) coacervates showed that both polymers were present within the coacervate phase surrounding the oil droplet, with substantial overlap in the merged channel (Fig. 3A).[26]

Encapsulation efficiency and droplet stability depend on the charge ratio Z, total polymer concentration, ionic strength, and pH. Raising salt concentration weakens complexation and lowers loading.[24] Excess salt can even dissolve pre-formed coacervates, reducing payload retention.[27] Mechanical robustness scales with the coacervates' viscoelastic modulus and interfacial elasticity and is typically increased by higher (bio)-polymer concentration, limited multivalent counterions, or adding a secondary network. After formation, capsules can be fixed by mild routes such as thermal setting of proteins or transglutaminase-mediated crosslinking, calcium-induced gelation of anionic polysaccharides, or controlled drying, which stabilise the morphology and limit coalescence, leakage, and oxygen transport.[28]

Complex coacervates are effective protectants for heat-labile ingredients. Microscopy of protein–polysaccharide coacervates confining probiotic bacteria across pH changes confirmed the formation of compact coacervates that persist for at least 24 h. Live–dead staining after thermal challenges demonstrated a protection gradient: non-encapsulated and peripheral cells were inactivated, whereas cells embedded within the coacervates remained largely viable (Fig. 3B).[29–31] Together, these studies show that complex coacervation enables high payloads under mild conditions and can improve survival or retention of sensitive ingredients once the liquid shell is promptly fixed into a shell of matrix appropriate for storage.

Complex coacervation represents only one route to structural heterogeneity in food systems. In many conventional food matrices, heterogeneity instead arises from gel matrix-guided segregative partitioning of macromolecular components during processing. For example, in yogurt fermented with exopolysaccharide (EPS)-producing lactic acid bacteria, confocal microscopy revealed a protein network containing EPS-enriched serum microdomains (Fig. 4A). Stirring altered the domain size and redistributed EPS, yet the overall compositional

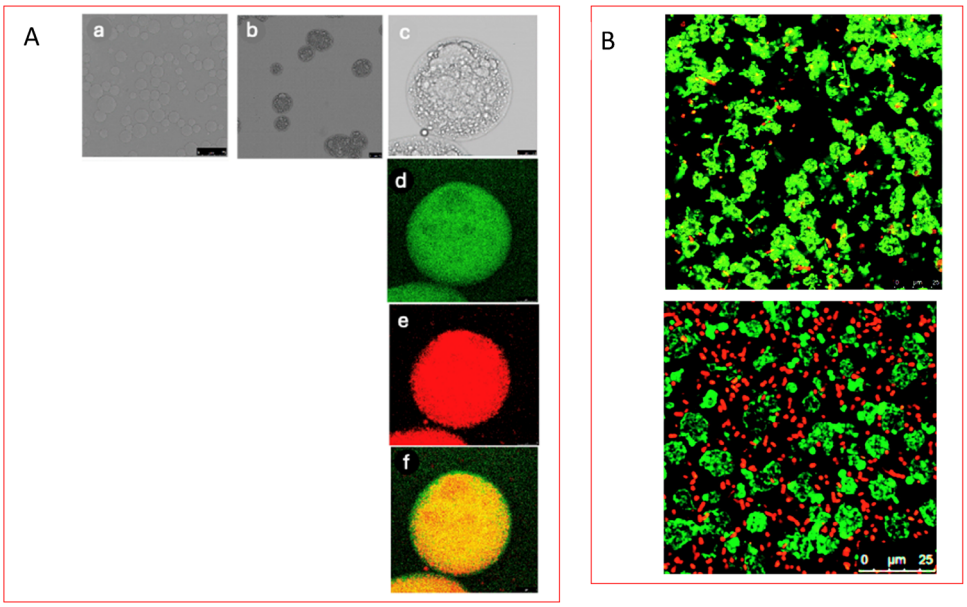

Fig. 3 Complex coacervation for encapsulation. (A) Gelatin-carboxymethyl cellulose (CMC) coacervates. (a) Unloaded; (b)–(f) loaded with conjugated linoleic acid; (d) FITC-labelled gelatin (green); (e) RBITC-labelled CMC (red); (f) merged green/red channels indicate both polymers are uniformly distributed, with a higher density of gelatin at the surface. (A) Adapted from ref. 26, *Food Hydrocolloids*, 2018, **80**, 149–159. DOI: https://doi.org/10.1016/j.foodhyd.2018.02.011, with permission from Elsevier, copyright 2018. (B) Thermal challenge of probiotic-loaded WPI–GA coacervates. Two fluorescent dyes were used: green labels all cells, and red labels only dead cells. After heating, non-encapsulated and peripheral cells are largely inactivated, whereas cells embedded within the coacervates remain viable. (B) Adapted from ref. 31, *Curr. Opin. Colloid Interface Sci.*, 2017, **28**, 96–109. DOI: https://doi.org/10.1016/j.cocis.2017.03.006, with permission from Elsevier, copyright 2017.

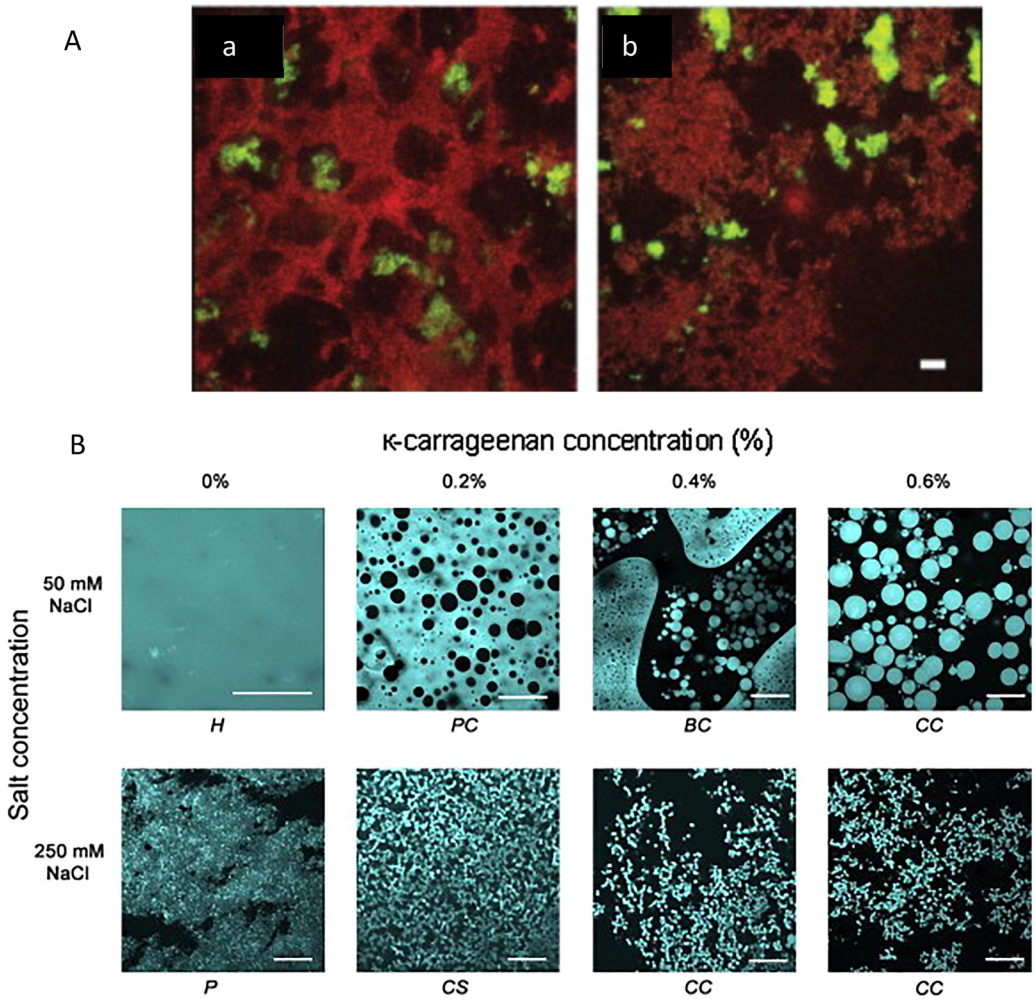

Fig. 4 Segregative partitioning and process-driven LLPS in foods. (A) Confocal laser scanning microscopy (CLSM) of yogurt fermented with exopolysaccharide (EPS)-producing lactic acid bacteria shows segregative partitioning. (a) Unstirred yogurt and (b) stirred yogurt. Protein (red), EPS (green); serum appears dark. Identical magnification used for (a) and (b). Scale bar: 10 μm. (A) Adapted from ref. 32, *J. Dairy Sci.*, 2003, **86**(5), 1632–1638. DOI: https://doi.org/10.3168/jds.S0022-0302(03)73748-5, with permission from Elsevier, copyright 2003. (B) CLSM of whey protein isolate(WPI)–κ-carageenan mixed gels. Bright = protein network; dark = carrageenan/serum. Scale bar: 50 μm. Gels were formed from 13 wt% protein WPI solutions containing 0–0.6 wt% κ-carrageenan. At 50 mM NaCl, the microstructure evolves from homogeneous (H) (0%) → protein-continuous (PC) (0.2%) → bicontinuous (BC) (0.4%) → carrageenan-continuous (CC) (0.6%). At 250 mM NaCl, WPI alone forms a particulate (P) network; adding carrageenan yields coarse-stranded (CS) (0.2%) and CC (0.4–0.6%), evidencing network inversion with increasing carrageenan and salt. (B) Adapted from ref. 33, *Food Hydrocolloids*, 2012, **29**(1), 234–245. DOI: https://doi.org/10.1016/j.foodhyd.2012.02.006, with permission from Elsevier, copyright 2012. Mixtures were homogeneous before heating. Upon heating transient segregative LLPS could initiate prior to or overlap with protein gelation and the evolving morphology became arrested in the gel.[33,34]

partitioning persisted.[32] Unlike LLPS, which involves two coexisting liquid (polymer) phases present before gelation, such segregative partitioning emerges as the matrix sets (*e.g.*, during protein gelation).

In addition to matrix-guided partitioning, heterogeneity can arise from process-driven LLPS. For example, whey protein isolate (WPI)–κ-carrageenan mixtures (13 wt% WPI with up to 0.6 wt% κ-carrageenan) are single-phase before heating ($\leq$45 °C). Upon heating to induce protein gelation, protein denaturation and aggregation, together with κ-carrageenan-induced depletion interactions, increase thermodynamic incompatibility, and can shift the formulation into the segregative two-phase region (across the binodal). This produces LLPS before that gelation arrests the demixed morphology (Fig. 4B).[33,34,38]

3. Food structuring by coacervation

3.1. Flow behaviour

Complex coacervates behave as viscoelastic liquids whose flow properties can be tuned and exploited for food structuring. At low shear rates, the apparent viscosity is nearly constant (near-Newtonian), reflecting undeformed, Brownian droplets. This behaviour has been reported for β-lactoglobulin–lactoferrin coacervates[7] up to $\sim$10 s^{-1} and for whey protein–gum

arabic coacervates[8] up to ~30 s^{-1}. The viscosity of such coacervates can be exceptionally high, up to 2500 times greater than that of individual biopolymer solutions at equivalent total concentration, due to dense internal structure and reversible electrostatic associations.[7,35]

As shear increases, droplets deform and align, increasing interfacial area, and reorganising the dispersed phase. This structural evolution produces pronounced shear-thinning. The apparent viscosity typically decreases by one to two orders of magnitude (~10–100 times) between low- and high-shear regimes.[7,8,36] When the shear rate is abruptly reduced and maintained within the low-shear Newtonian regime, the viscosity does not adjust instantaneously to its new steady-state value. Instead, the apparent viscosity increases gradually as droplets relax toward the spherical shape, inter-droplet contacts reform, and transient networks are re-established, consistent with thixotropic behaviour at sufficiently low shear rates.[7,36] This reversible shear-thinning and recovery define the processing window of coacervate dispersions.

For simple shear at low Reynolds number and volume fractions $0 < \phi < \phi_{max}$, the bulk viscosity of a liquid coacervate dispersion can be described using the Faroughi–Huber deformable-droplet framework.[37] The model treats the system as deformable droplets dispersed in a continuous matrix. Coacervate dispersions satisfy this description, with the serum acting as the matrix phase and the coacervate–serum interfacial tension providing the restoring capillary stress.

In simple shear, the capillary number is calculated as follows[37]

$$\mathrm{Ca}(\dot{\gamma}) = \frac{\dot{\gamma} \times \eta_m(\dot{\gamma}) \times R_c}{\Gamma_{cs}} \quad (2)$$

where $\dot{\gamma}$ is the shear rate (s^{-1}), $\eta_m(\dot{\gamma})$ is the serum (matrix) apparent viscosity (Pa s), R_c is a characteristic coacervate droplet radius, and Γ_{cs} is the coacervate–serum interfacial tension (typically 1–100 μN m^{-1}.[22,23]). The capillary number Ca compares viscous stress ($\dot{\gamma}\eta_m$) to capillary stress (Γ/R_c). The viscosity ratio is[37]

$$\lambda(\dot{\gamma}) = \frac{\eta_c(\dot{\gamma})}{\eta_m(\dot{\gamma})} \quad (3)$$

where $\eta_c(\dot{\gamma})$ is the apparent viscosity of the coacervate (dispersed) phase. Together Ca, λ, and ϕ determine the dispersion's relative and bulk viscosities in the Faroughi–Huber model. Formulation variables such as salt, pH, and charge ratio alter $\eta_c(\dot{\gamma})$, Γ_{cs}, and ϕ, thereby, the extent of shear-thinning and the rate of recovery are programmable by formulation.

Within this framework, the relative viscosity $\eta_r = \frac{\eta_{bulk}}{\eta_m}$ is defined as:[37]

$$\eta_r \times \left(\frac{N + M\kappa \mathrm{Ca}^2 (\eta_r)^2}{N + M\kappa \mathrm{Ca}^2}\right)^{\frac{1}{2}\left(\frac{N}{M}-1\right)} = \left(\frac{\phi_m - \phi}{\phi_m \times (1-\phi)}\right)^{-N \times \frac{\phi_m}{1-\phi_m}} \quad (4)$$

where ϕ_{max} = 0.64 is the maximum packing fraction, and the coefficients N, M and κ depend on λ as specified in eqn (5)–(7).[37]

$$N = \frac{1 + 2.5 \times \lambda}{1 + \lambda}, \quad (5)$$

$$M = 140 \times \frac{\lambda^3 + \lambda^2 - \lambda - 1}{28 \times (2 \times \lambda + 3) \times (\lambda + 1)^2}, \quad (6)$$

$$\kappa = \left((2 \times \lambda + 3) \times \frac{19 \times \lambda + 16}{40 \times (\lambda + 1)}\right)^2 \quad (7)$$

At high Ca (fixed λ, ϕ and Γ_{cs}) droplets become strongly deformed and aligned. If breakup and coalescence are negligible, so that ϕ remains constant, further increase in Ca produces only weak additional shear-thinning and η_{bulk} varies slowly with $\dot{\gamma}$. If breakup dominates, η_{bulk} decreases further with $\dot{\gamma}$. Under coalescence-dominated conditions, η_{bulk} may increase.

Experimentally, $\eta_m(\dot{\gamma})$ is obtained by viscometry of the serum (matrix) phase, R_c by microscopy (ideally the Sauter mean radius R_{32}), and Γ_{cs} by spinning-drop tensiometry. The coacervate phase viscosity $\eta_c(\dot{\gamma})$ can be estimated by (i) direct rheometry of the isolated dense phase, collected by gentle settling,[7] (ii) fitting single-droplet deformation or relaxation under controlled shear in a rheo-optical or microfluidic cell,[22] or (iii) microrheology using tracer diffusion, and the Stokes–Einstein relation to obtain zero-shear viscosity.[38] Microrheology yields the zero-shear dynamic viscosity from Brownian motion, which may differ from the apparent shear-rate-dependent viscosity required in $\lambda(\dot{\gamma})$.

3.2. Coacervate-derived hydrogels

Liquid coacervates form most readily when the participating proteins are soluble (not aggregated) prior to complexation. Moderate pre-heating can expose hydrophobic domains and reactive groups (*e.g.*, thiols) without causing bulk aggregation. This increases the number of accessible interaction sites and accelerates network formation upon mixing with a coacervating partner, and can shift or narrow the coacervation window, for example, by increasing salt sensitivity.[39] More extensive pre-heating can promote irreversible aggregation, and where reactive groups are available, covalent crosslinking. In such cases, phase separation may coincide with the formation of a percolated network,[4] with gel-like[40] or viscoplastic behaviour rather than freely flowing droplet dispersion (Fig. 5A).

Even when coacervates exhibit liquid-like rheology, the dispersion is inherently metastable with respect to coalescence. The droplets persist because interfacial tension and viscous resistance slow fusion, not because it represents a thermodynamic minimum. As the dispersion ages, inter-droplet contacts promote drainage of the intervening serum, rupture of the interface, and fusion into larger droplets. Interfacial tension then drives capillary relaxation toward spherical shape. The magnitude of the coacervate–serum interfacial tension (Γ_{cs}) determines the capillary drive for rounding, whereas the dense-phase viscosity (η_c) governs film drainage and interface healing.

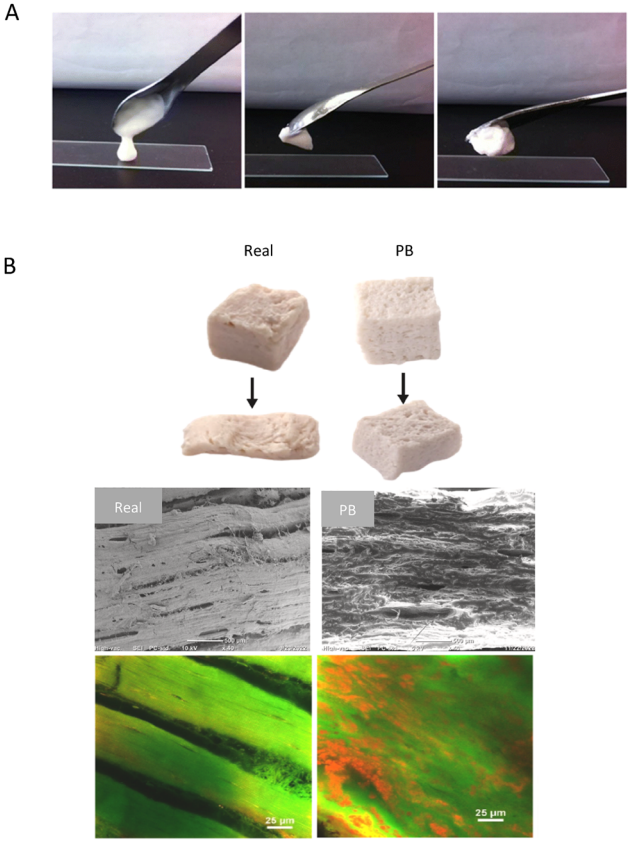

Fig. 5 Coacervation as a texturizing/structuring tool. (A) Effect of protein pre-heating on complexation: gum arabic–soy protein mixtures form liquid coacervates when proteins remain largely native (left panel), whereas pre-heating to 85 °C and 95 °C yields percolated, solid-like aggregates (middle and right panels). (A) Adapted from ref. 4, *Soft Matter*., 2024, **20**(9), 1966–1977. DOI: https://doi.org/10.1039/D3SM01275A, licensed under the Creative Commons CC-BY 3.0 licence, copyright 2024. (B) Flow-templated structuring for meat analogues (potato protein–gellan with vegetable oil). Coacervation concentrates protein, gentle shear aligns the droplet/interfacial phase, and subsequent thermal/ionic setting fixes the architecture into a fibrous gel. Macroscopic compression images and microscopy (protein in green; lipid in red) show a directional, layered structure in a plant-based (PB) system compared with real chicken. (B) Adapted from ref. 43, *Food Hydrocolloids*, 2023, **142**, 108817. DOI: https://doi.org/10.1016/j.foodhyd.2023.108817, with permission from Elsevier, copyright 2023.

Under quiescent and chemically static conditions, repeated droplet contacts lead to progressive coalescence, increasing the mean droplet size and reducing droplet count. When connectivity exceeds a critical threshold, a space-spanning network forms and the dense phase becomes continuous, yielding a proto-gel. This percolation-*via*-coalescence is the basis of coacervate-derived hydrogel formation.[41]

Ionic strength, pH, and multivalent ions modulate inter-droplet attraction, while mixing and flow history determine the initial droplet size distribution and collision frequency. Temperature further affects both phase properties and rheological behaviour. In a gelatin–gum arabic system, lowering the phase separation temperature from 40 °C to 10 °C produced a denser, more viscous coacervate, broadened the low-shear Newtonian plateau, and enhanced shear-thinning. At 10 °C the dense phase behaved predominantly viscously at low angular frequency but exhibited a G'/G'' crossover above $\sim$73 rad s^{-1}, indicating elastic dominance at high ω. Further cooling to 3 °C yielded a weak gel with $G' > G''$ across the entire frequency range.[42]

When subjected to shear, coacervate droplets can act as flow-templated deformable intermediates for anisotropic food structures, including meat analogues. In potato protein–gellan systems containing vegetable oil,[43] the ultralow coacervate–serum interfacial tension,[22] permitted substantial droplet deformation under modest shear. When deformation was arrested before relaxation, the elongated droplets were preserved, yielding flow-aligned, anisotropic textures (Fig. 5B). Arrest can be induced by thermal setting, enzymatic cross-linking, addition of multivalent ions, or controlled dehydration, producing a fibrous viscoelastic network with directional mechanical response and tear resistance. Inclusion of dispersed oil during the liquid stage[43] further increases alignment as the coacervate spreads over oil droplets, and once set, these inclusions contribute to composite architecture and mechanical anisotropy.

4. Food structuring by segregative LLPS

4.1. Segregatively phase-separating food polymers

Segregative LLPS in biopolymer systems has been reviewed extensively in food science, particularly in the context of ATPS and protein separation technologies.[44,45] Numerous food-grade biopolymer combinations can induce incompatibility-driven demixing. Foundational reviews document protein–polysaccharide, protein–protein, and polysaccharide–polysaccharide ATPS pairs across defined composition, pH, ionic strength, and temperature conditions.[46–48]

For protein–neutral polysaccharide systems (*e.g.*, dextran, amylopectin, and polysucrose), demixing typically occurs near the protein isoelectric point (pI) at low ionic strength and extends over a broader pH range as salt screens residual electrostatic attraction. With carboxylated polysaccharides (pectin, alginate, CMC, and gum arabic), incompatibility generally appears at pH values above the protein pI and is enhanced by moderate ionic strength.[46,48] Segregative demixing has also been reported for whey protein isolate (WPI)–CMC under isoionic conditions, where ionic strength arises solely from polymer counterions, demonstrating that the added electrolyte is not required to trigger demixing.[49] Heating and modification of proteins can be used to induce incompatibility with co-charged polysaccharides. While native whey proteins and heat-treated whey proteins did not segregatively demix with alginate under typical conditions, combined heating and lysine acetylation promoted demixing. This yielded alginate-in-protein aqueous two-phase emulsions.[50] Sulphated polysaccharides (*e.g.*, dextran sulphate) generally remain compatible with proteins at low ionic strength but demix at elevated

Table 1 Typical demixing conditions for protein–polysaccharide pairs

	Polysaccharide		
	Neutral	Carboxylated	Sulphated (dextran sulfate)
Albumins	Near pI at low salt; at pH ≠ pI when salt is high	pH > pI, salt widens the demixing window (moderate ionic strength)	Often compatible at low salt; demixing appears only at higher pH and salt (applies to all protein classes)
Globulins	Slightly alkaline pH with added salt; incompatibility increases with ionic strength	Alkaline pH + moderate salt	
Caseins	Near-neutral pH with moderate salt	Alkaline pH; alginate: near neutral pH + salt	
Prolamins/ glutelins	Mainly under alkaline + salted conditions	Alkaline pH; demixing enhanced by salt	

Demixing boundaries are system-specific and shift with molecular weight distribution, total polymer concentration, and processing history. Salt refers to monovalent electrolytes.

pH and salinity.[46,48] Table 1 summarises representative protein–polysaccharide demixing conditions as a screening guide rather than rigid boundaries. Exact demixing boundaries depend on molecular weight distribution, compositional heterogeneity, and processing history.

Binary protein–protein mixtures rarely undergo segregative LLPS. Under common processing conditions, they tend to co-aggregate or exhibit associative microphase separation rather than macroscopic demixing.[51] Apparent two-phase morphologies typically reflect pre-existing large aggregates (especially in some commercial plant isolates) rather than incompatibility between native proteins. In practice, segregative demixing emerges mainly when one partner is pre-aggregated or extensively denatured,[52] as observed for gelatin mixed with polymerised (heat-aggregated) whey protein.[53]

Beyond protein–polysaccharide pairs, mixtures of unlike polysaccharides can undergo segregative LLPS, under mild, food-relevant conditions. Phase behaviour is governed by each polymer's charge density and distribution, degree of esterification or substitution, molecular weight, and solution pH and ionic strength. For example, alginate–sugar–beet pectin systems demixed near-neutral pH at low-to-moderate salt concentrations, with solute partitioning strongly influenced by the pectin's degree of esterification and compositional heterogenity.[54]

4.2. The elongation–arrest process

Segregative LLPS enables the formation of anisotropic textures through controlled deformation arrest. The process involves three coupled steps: formation of a W/W (ATPS) emulsion under conditions favouring thermodynamic incompatibility; deformation and alignment of dispersed domains under shear; and rapid solidification of one or both phases to preserve the deformed morphology.[55] The resulting gels retain a characteristic length scale determined by domain size at the moment of arrest, which governs fibre thickness, spacing, and directional mechanical response. Confocal imaging of dextran–gelatin methacryoyl ATPS gels set immediately after shear (Fig. 6A) shows the importance of initial morphology. Starting from a bicontinuous mixture (at $\dot{\gamma}$ = 0 s^{-1}), increasing shear produced flow-aligned string-like domains. When starting from a droplet-in-matrix emulsion, strong shear produced parallel droplet lanes separated by matrix-rich bands. At $\dot{\gamma}$ = 100 s^{-1}, the whole-disk view of the bicontinuous system shows circumferential alignment imposed by the rotational shear field, indicating that processing geometry determines fibre orientation. Band spacing decreases with increasing $\dot{\gamma}$ and is preserved upon arrest. At $\dot{\gamma}$ = 1 s^{-1}, alignment is weak, consistent with a threshold shear rate and residence time before arrest.[56] This ''mix–shear–arrest'' strategy is compatible with standard food unit operations such as mixers, and scraped-surface heat exchangers.

High-temperature shear demonstrates the coupling between flow and phase structure under processing-relevant conditions. In a conical shear cell at ~140 °C, soy protein isolate (SPI) blended with pectin exhibited shear-dependent morphology: without shear, the set product was isotropic with randomly distributed pores; at ~39 s^{-1} the mixture formed layered, fibrous sheets with pores elongated along the shear direction (Fig. 6B). Volumetric reconstructions of the entrained air confirm the imposed alignment. Under identical conditions, SPI alone produced larger, less continuous lamellar structures.[57] These results indicate that the addition of a segregating polysaccharide promotes phase separation under shear and yields finer, more continuous aligned domains after set. They also demonstrate that the imposed shear field and processing geometry determine final orientation.

High-moisture extrusion of soy protein concentrate (SPC)–wheat gluten (WG) mixtures follows the same ''demixing–alignment–arrest'' sequence. At ≈57% moisture, fibrosity increased as WG content increased from 0 to 10, 20 and 30% on a dry basis (Fig. 6C). The reported interpretation emphasised protein denaturation together with hydrogen bonding and disulphide crosslinking during processing.[58] However, studies on soy protein isolate (SPI)–WG studies at comparable solid contents show that these mixtures are already biphasic after simple mixing, comprising a soy-rich, more-hydrated phase and a gluten-rich, less-hydrated phase. TD-NMR measurements indicated negligible diffusive exchange and stable water partitioning under heating and shear.[59,60] These observations suggest that SPC–WG systems should be viewed as pre-existing, water-partitioned protein blends that undergo flow-induced

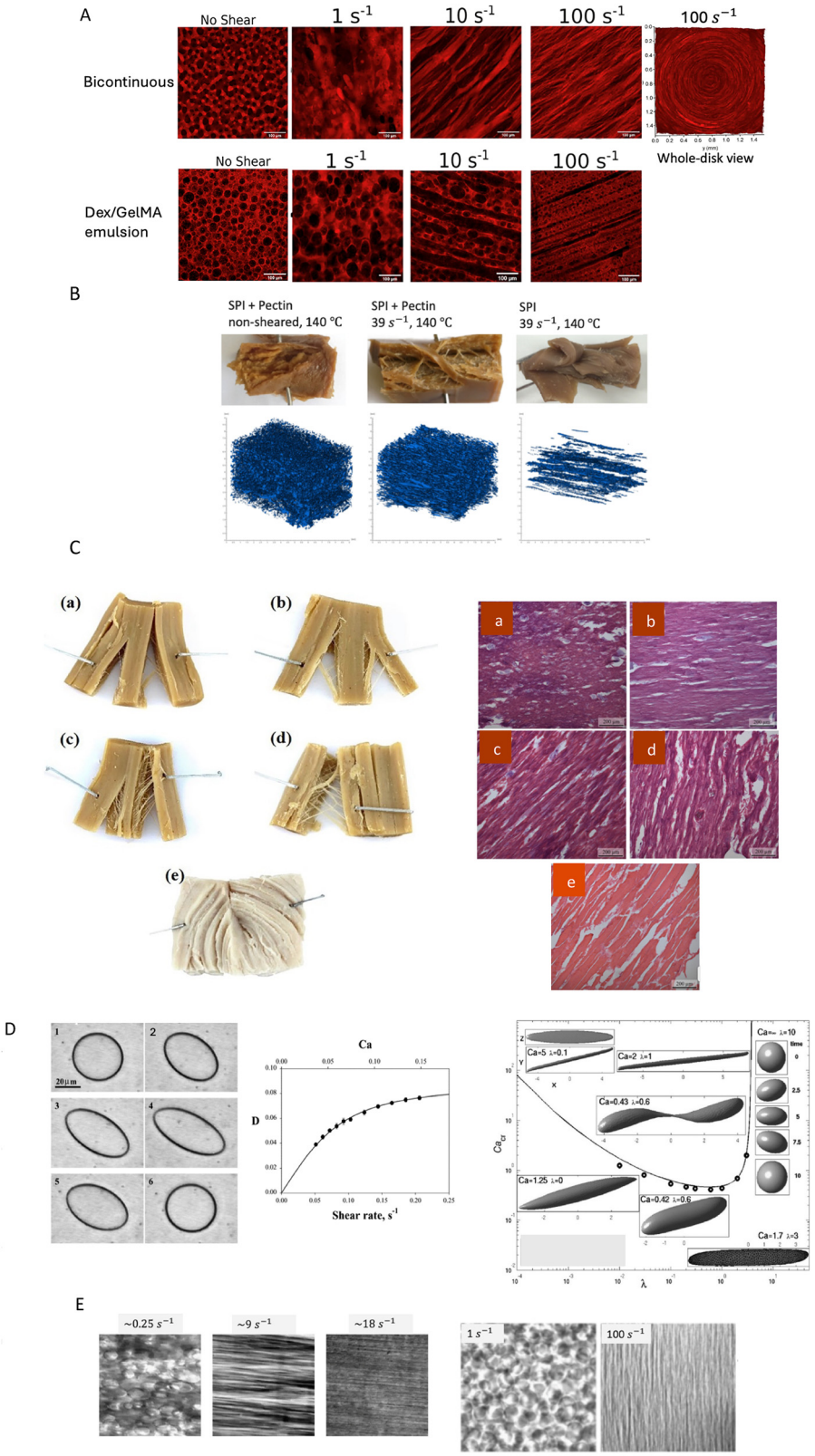

Fig. 6 Flow-templated structuring by LLPS and segregative partitioning across scales. (A) Bicontinuous *vs.* droplet morphologies in a model ATPS. Confocal images of dextran–gelatin methacryoyl (GelMA) mixtures set immediately after shear. A bicontinuous composition develops flow-aligned fibrils as $\dot{\gamma}$ increases; a droplet-in-matrix emulsion forms droplet lanes separated by matrix-rich bands at high $\dot{\gamma}$. Whole-disk view shows circumferential alignment from the rotational shear field. (A) Adapted from ref. 56, *Soft Matter*, 2024, **20**(4), 773–787. DOI: https://doi.org/10.1039/D3SM01365K, with permission from The Royal Society of Chemistry, copyright 2024. (B) Shear cell setting of protein–polysaccharide ATPSs. At 140 °C, soy protein isolate (SPI) with pectin without shear is isotropic; at $\dot{\gamma} \approx 39\ s^{-1}$ it forms layered, fibrous sheets. SPI alone at the same conditions yields larger, more

discontinuous laminae. 3D reconstructions of entrained air (blue) visualize flow-induced alignment. (B) Adapted from ref. 57, *J. Food Eng.*, 2018, **222**, 84–92. DOI: https://doi.org/10.1016/j.jfoodeng.2017.11.014, with permission from Elsevier, copyright 2018. (C) Soy protein concentrate (SPC)–wheat gluten (WG) blends: pre-existing segregative protein–protein phase separation. High-moisture extrusion (~57% water) of SPC–WG yielded progressively stronger fibrosity as WG content increased. The starting paste was a two-phase protein blend (soy-rich/gluten-rich) present before extrusion; flow in the die aligned these viscoelastic phases, and thermal/disulphide crosslinking arrested the aligned morphology. Visual (left) and light microscopy (right) images of chicken analogues (a)–(d) and (e) boiled chicken breast. Labels a–d correspond to rising WG content on the dry weight basis from 0 to 10, 20, and 30%, both before and after high-moisture extrusion. (C) is adapted from ref. 58, *Food Struct.*, 2019, **19**, 100102. DOI: https://doi.org/10.1016/j.foostr.2018.11.002, with permission from Elsevier, copyright 2019. (D) Single-drop deformation mechanism in segregative LLPS. Left: A nearly spherical caseinate droplet in an alginate phase elongates after a step to fixed $\dot{\gamma}$ and reaches a steady shape set by Ca and λ. The deformation parameter $D = (L - S)/(L + S)$ increases with $\dot{\gamma}$ and then plateaus. Right: Grace map of critical capillary (Ca_{cr}) *versus* viscosity ratio λ (log–log) with example shapes. A high λ sequence (right inset) shows weak deformation and capillary-driven relaxation toward a sphere. (D) Left panel was adapted form from ref. 61, *Carbohydr Polym.*, 2002, **48**(2), 143–152. DOI: https://doi.org/10.1016/S0144-8617(01)00220-X, with permission from Elsevier, copyright 2002. (D) Right was adapted from ref. 62, *Colloid Interface Sci Commun.*, 2022, **47**, 100597. DOI: https://doi.org/10.1016/j.colcom.2022.100597, with permission from Elsevier, copyright 2022. (E) String-phase formation at low λ. In segregative LLPS systems with low λ and a sufficiently viscous matrix, elongated threads persist under flow; increasing $\dot{\gamma}$ sharpens alignment. Examples shown for pullulan–sodium dodecyl sulphate (SDS) and gelatin–dextran systems. (E) Was adapted from ref. 70, *Food Hydrocolloids*, 2008, **22**(1), 121–129. DOI: https://doi.org/10.1016/j.foodhyd.2007.04.016, with permission from Elsevier, copyright 2008.

alignment in the die, followed by fixation by thermal and disulphide crosslinking.

4.3. Mechanistic controls on the in-flow deformation–arrest

Single-drop experiments (Fig. 6D) provide direct insight into shear-induced deformation. Following a step to a fixed $\dot{\gamma}$, an initially spherical droplet elongates transiently and reaches a steady deformation determined primarily by the capillary number Ca and viscosity ratio λ.[61] Fig. 6D summarizes how Ca and λ jointly govern droplet deformability and the breakup in Newtonian liquids such as dilute emulsions. At fixed volume, fraction ϕ, increasing Ca (stronger viscous stress) or decreasing λ promotes elongation. Conversely, large λ suppresses deformation and increases the critical Ca for breakup, Ca_{cr}. The dependence of Ca_{cr} on λ follows the so-called 'Grace curve', which spans $\lambda \ll 1$ to $\lambda \gg 1$. The minimum Ca_{cr} occurs at $\lambda \approx 0.1$–1 and increases for both very small and very large λ (Fig. 6D).[62]

For non-Newtonian systems such as ATPS droplets, the Grace curve provides only a first-order reference. Matrix elasticity, yield stress and interfacial mobility alter the deformation and breakup criteria. In such cases, capillary and elastic stresses compete, and deformation is governed jointly by Ca and the Weissenberg number Wi (or equivalently, the Deborah number De). In steady shear, the matrix-based Weissenberg number is defined as

$$\mathrm{Wi} \equiv \dot{\gamma}\tau_{\mathrm{mat}} \tag{8}$$

where τ_{mat} is the longest linear viscoelastic relaxation time[63] of the stress-bearing phase. De is defined as $\mathrm{De} \equiv \tau/t_{\mathrm{f}}$, where τ is a characteristic relaxation time and t_{f} is the characteristic flow timescale.[64] For steady shear, taking $t_{\mathrm{f}} = 1/\dot{\gamma}$ and $\tau = t_{\mathrm{mat}}$ gives De = Wi. The relaxation time quantifies stress memory, that is, the persistence of elastic stresses generated during deformation after a change in $\dot{\gamma}$. Expressed as $\mathrm{Wi} = \frac{\tau_{\mathrm{mat}}}{t_{\mathrm{f}}}$, when Wi ($\gtrsim 1$), the deformation occurs on a timescale shorter than stress relaxation.[64,65] Consequently, elastic stresses remain partially unrelaxed and influence the droplet shape and breakup. When Wi $\ll$ 1, stresses relax rapidly during deformation, and Newtonian capillary-based descriptions provide an adequate baseline. Importantly, elastic modulus and elastic relaxation time are distinct quantities; a large elastic modulus does not imply long stress memory.

The material relaxation time τ_{mat} can be estimated from small-amplitude oscillatory shear (SAOS) measurements of the isolated phase. For systems that are well described by a single-mode Maxwell model, $\tau_{\mathrm{mat}} \approx 1/\omega_{\mathrm{cross}}$, where ω_{cross} is the lowest frequency at which $G' = G''$.[66] An alternative estimate is $\tau_{\mathrm{mat}} \approx \eta_0/G_0$, where η_0 is the zero-shear viscosity[67] obtained from creep, stress-relaxation, or SAOS measurements, and G_0 is the elastic modulus obtained from linear viscoelastic measurements.

Droplet deformation under shear is quantified by the Taylor parameter

$$D = \frac{(L - S)}{(L + S)} \tag{9}$$

where L and S are the instantaneous semi-major (long) and semi-minor (short) axes from ellipse fits to the drop counter. Under steady shear, D increases with $\dot{\gamma}$ (hence with Ca), and then plateaus (Fig. 6D), indicating an approach to a steady elongated shape and orientation distribution.[61]

Following shear cessation, capillary pressure (Γ/R_{d}) drives the droplet back toward a sphere, while the induced creeping flow is dissipated predominantly by viscous loss in the continuous (matrix) phase. The characteristic relaxation time can therefore be approximated using the equation developed for small deformations of an unconfined Newtonian droplet:[68]

$$\tau_{\mathrm{shape}} \approx \frac{\alpha\eta_{\mathrm{m}}R_{\mathrm{d}}}{\Gamma_{\mathrm{w-w}}}, \tag{10}$$

$$\alpha = \frac{(2\lambda + 3)(19\lambda + 16)}{40(\lambda + 1)} \tag{11}$$

where R_{d} is the droplet radius, and $\Gamma_{\mathrm{w-w}}$ is the water–water interfacial tension (typically 1–100 μN m^{-1} for ATPSs).[69] Because relaxation occurs without imposed shear, and both phases in ATPSs are generally viscoelastic, η_{d} and η_{m} should be taken as zero-shear viscosities when estimating λ for use in eqn (11).

At the bulk scale, shear can promote topological transitions and reorganize microstructure. When the dispersed phase is much less viscous than the matrix ($\lambda \ll 1$) and the matrix viscosity is sufficiently high, droplets elongate into continuous threads, forming a ''string'' (Fig. 6E). Low-λ conditions also favour shear-induced phase inversion, where the less-viscous phase percolates and becomes continuous. Both string formation and inversion typically lower the apparent viscosity (*via* alignment and reduced hydrodynamic hindrance), and are reversible (with hysteresis) upon cessation of shear. The observed morphology during flow, including isolated elongated droplets, string, and inversion depend on λ, dispersed phase volume fraction ϕ, matrix viscosity η_m, and accumulated strain. Low λ and sufficiently high η_m are necessary for sustained thread formation; if the matrix is not viscous enough, breakup dominates even when $\ll 1$.[70] At higher ϕ and with larger accumulated strain, droplets coalesce laterally into longer domains that are more uniformly oriented along the flow, and the microstructure becomes more anisotropic (Fig. 6E). Near the inversion threshold, modest changes in $\dot{\gamma}$ or ϕ can switch which phase is continuous.[70,71]

The fibre thickness fixed at arrest reflects the characteristic domain size at the moment solidification occurs. It is determined by (i) the balance between flow-induced viscous stretching and capillary restoration together with elastic stress memory (quantified by Wi or De) that delays relaxation and can stabilise elongated shapes, and (ii) the accumulated shear strain prior to arrest. Viscous deformation scales with Ca, whereas capillary relaxation scales with Γ/R. Elastic stress memory, quantified by Wi delays relaxation and can stabilise elongated domains. The viscosity ratio λ further modulates deformability and the breakup threshold.

Although quantitative ''anisotropy *vs.* Wi '' maps for ATPSs (segregative LLPS) and coacervates (associative LLPS) are still scarce, it is well established that greater accumulated shear strain ($\gamma = \dot{\gamma}t$, with t = time under shear), and higher Ca enhance elongation and alignment.[63,72–74] Structural anisotropy is preserved when arrest occurs on a timescale shorter than shape relaxation.

The orientational anisotropy (*i.e.*, the degree of alignment of elongated domains with the flow direction) can be quantified using Herman's orientation factor:[75]

$$f = \frac{1}{2}\left(3\langle \cos^2\theta \rangle - 1\right) \quad (12)$$

where θ is the angle between a domain's long axis and the flow direction (reference axis), and $\langle\cdot\rangle$ denotes an average over domains. Herman's orientation factor is defined for 3D orientation distributions and has been used recently to track the orientation degree of nanofibrillar networks along the stretching direction in anisotropic polyvinyl alcohol/cellulose hydrogels.[76] Herman's factor is commonly obtained from the azimuthal intensity distribution (intensity *vs.* angle on the detector) of (ultra)small angle scattering patterns by calculating $\langle \cos^2\theta \rangle$, assuming axial symmetry around the reference axis. For 2D image analysis of elongated domains, an in-plane orientation index can be used:

$$O_{2D} = 2\langle \cos^2\varphi \rangle - 1, \quad (13)$$

with φ is the in-plane angle between a structural feature (elongated domains) and a reference axis (typically the flow direction).[77] In this convention $O_{2D} \to 0$ indicates high isotropy, and $O_{2D} \to 1$ corresponds to perfect alignment parallel to the flow.

5. Conclusions

LLPS is best treated as a coupled thermodynamic and hydrodynamic problem in which phase separation, flow-induced deformation, and arrest kinetics determine the structure. When deformation outpaces capillary and viscoelastic relaxation, domains elongate and align; when relaxation dominates, structures revert or coarsen. The capillary number Ca, viscosity ratio λ, matrix viscosity (η_m), and viscoelastic relaxation time of the stress-bearing phase govern this balance. Their interplay manifests in shear-thinning, droplet elongation, alignment, and at sufficient accumulated strain, string-like domain formation. Framed this way, ''mix–shear–set'' provides a general processing route: impose controlled deformation while domains are fluid, then arrest the morphology thermally, enzymatically, ionically, or by controlled dehydration. Solvent quality, ionic strength, temperature, shear history, and arrest timing set the accessible length scale and structural anisotropy.

Quantitative control requires linking measurable parameters to deformation and arrest thresholds. Ca and Wi define the relative contributions of viscous, capillary, and elastic stresses. Image-derived orientation metrics, including Herman's orientation factor, quantify domain alignment. Droplet-scale step-shear or extension tests resolve deformation and relaxation kinetics that are not accessible from bulk rheology. Together, these measurements position a formulation within the deformation–relaxation–arrest framework and constrain the structural outcomes under a given process history.

Significant constraints remain. Food-grade polymers are polydisperse and structurally heterogeneous, and prior thermal or mechanical history shifts demixing boundaries and kinetics. Interfacial tensions in ATPSs are ultralow, yet insufficiently characterised across realistic composition windows. Ageing, syneresis, and solute migration further complicate long-term stability, while quantitative *in situ* measurements under flow remain limited. Advancing the field requires systematic formulation maps spanning composition, temperature, and ionic strength; standardised measurement of ultralow interfacial tension and viscoelastic relaxation; direct coupling of imaging with rheology to bridge droplet-scale dynamics and bulk response; and scale-up studies that preserve control over arrest timing and phase inversion.

Conflicts of interest

There are no conflicts to declare.

Data availability

No primary research results, software or code have been included and no new data were generated or analysed as part of this review.

References

1 C. E. Sing, Development of the modern theory of polymeric complex coacervation, *Adv. Colloid Interface Sci.*, 2017, **239**, 2–16, DOI: 10.1016/j.cis.2016.04.004.
2 N. Martin, Dynamic Synthetic Cells Based on Liquid–Liquid Phase Separation, *ChemBioChem*, 2019, **20**(20), 2553–2568, DOI: 10.1002/cbic.201900183.
3 M. Abbas, W. P. Lipiński, J. Wang and E. Spruijt, Peptide-based coacervates as biomimetic protocells, *Chem. Soc. Rev.*, 2021, **50**(6), 3690–3705, DOI: 10.1039/D0CS00307G.
4 N. Doshi, W. Guo and F. Chen, *et al.*, Simple and complex coacervation in systems involving plant proteins, *Soft Matter*, 2024, **20**(9), 1966–1977, DOI: 10.1039/D3SM01275A.
5 S. Alberti, A. Gladfelter and T. Mittag, Considerations and Challenges in Studying Liquid–Liquid Phase Separation and Biomolecular Condensates, *Cell*, 2019, **176**(3), 419–434, DOI: 10.1016/j.cell.2018.12.035.
6 C. D. Keating, Aqueous Phase Separation as a Possible Route to Compartmentalization of Biological Molecules, *Acc. Chem. Res.*, 2012, **45**(12), 2114–2124, DOI: 10.1021/ar200294y.
7 R. Soussi Hachfi, M. H. Famelart, F. Rousseau, P. Hamon and S. Bouhallab, Rheological characterization of β-lactoglobulin/lactoferrin complex coacervates, *LWT*, 2022, **163**, 113577, DOI: 10.1016/j.lwt.2022.113577.
8 F. Weinbreck, R. H. W. Wientjes, H. Nieuwenhuijse, G. W. Robijn and C. G. de Kruif, Rheological properties of whey protein/gum arabic coacervates, *J. Rheol.*, 2004, **48**(6), 1215–1228, DOI: 10.1122/1.1795191.
9 J. Zheng, P. Van der Meeren and W. Sun, New insights into protein–polysaccharide complex coacervation: Dynamics, molecular parameters, and applications, *Aggregate*, 2024, **5**(1), e449, DOI: 10.1002/agt2.449.
10 A. Garaizar, J. R. Espinosa and J. A. Joseph, *et al.*, Aging can transform single-component protein condensates into multiphase architectures, *Proc. Natl. Acad. Sci. U. S. A.*, 2022, **119**(26), e2119800119, DOI: 10.1073/pnas.2119800119.
11 H. Tanaka, Viscoelastic phase separation, *J. Phys.: Condens. Matter*, 2000, **12**(15), R207–R264, DOI: 10.1088/0953-8984/12/15/201.
12 C. P. Brangwynne, P. Tompa and R. V. Pappu, Polymer physics of intracellular phase transitions, *Nat. Phys.*, 2015, **11**(11), 899–904, DOI: 10.1038/nphys3532.
13 D. Priftis and M. Tirrell, Phase behaviour and complex coacervation of aqueous polypeptide solutions, *Soft Matter*, 2012, **8**(36), 9396–9405, DOI: 10.1039/C2SM25604E.
14 A. A. Hyman, C. A. Weber and F. Jülicher, Liquid–Liquid Phase Separation in Biology, *Annu. Rev. Cell Dev. Biol.*, 2014, **30**(1), 39–58, DOI: 10.1146/annurev-cellbio-100913-013325.
15 S. F. Banani, H. O. Lee, A. A. Hyman and M. K. Rosen, Biomolecular condensates: organizers of cellular biochemistry, *Nat. Rev. Mol. Cell Biol.*, 2017, **18**(5), 285–298, DOI: 10.1038/nrm.2017.7.
16 R. V. Pappu, S. R. Cohen, F. Dar, M. Farag and M. Kar, Phase Transitions of Associative Biomacromolecules, *Chem. Rev.*, 2023, **123**(14), 8945–8987, DOI: 10.1021/acs.chemrev.2c00814.
17 M. Feric, N. Vaidya and T. S. Harmon, *et al.*, Coexisting Liquid Phases Underlie Nucleolar Subcompartments, *Cell*, 2016, **165**(7), 1686–1697, DOI: 10.1016/j.cell.2016.04.047.
18 X. Shi, Y. Li and H. Zhou, *et al.*, DDX18 coordinates nucleolus phase separation and nuclear organization to control the pluripotency of human embryonic stem cells, *Nat. Commun.*, 2024, **15**(1), 10803, DOI: 10.1038/s41467-024-55054-8.
19 D. C. Dewey, C. A. Strulson, D. N. Cacace, P. C. Bevilacqua and C. D. Keating, Bioreactor droplets from liposome-stabilized all-aqueous emulsions, *Nat. Commun.*, 2014, **5**(1), 4670, DOI: 10.1038/ncomms5670.
20 K. Chen, A. D. Troise, S. De Pascale, A. Scaloni, V. Fogliano and A. Madadlou, Compartmentalization vs. segregation of reactants: accomplishment of the Maillard reaction at the water-water interface, *Food Chem.*, 2025, **465**, 142089, DOI: 10.1016/j.foodchem.2024.142089.
21 K. Chen, A. D. Troise and A. Bunschoten, *et al.*, Natural Deep Eutectic Solvent–Dipotassium Phosphate Aqueous Two-Phase Systems: Physicochemical Characterization, Selective Partitioning of Amino Acids and Glucose, and Functional Insight into Maillard Reaction Applications, *ACS Sustainable Chem. Eng.*, 2025, **13**(30), 11898–11912, DOI: 10.1021/acssuschemeng.5c03053.
22 S. Ali and V. M. Prabhu, Characterization of the Ultralow Interfacial Tension in Liquid–Liquid Phase Separated Polyelectrolyte Complex Coacervates by the Deformed Drop Retraction Method, *Macromolecules*, 2019, **52**(19), 7495–7502, DOI: 10.1021/acs.macromol.9b01491.
23 V. M. Prabhu, Interfacial tension in polyelectrolyte systems exhibiting associative liquid–liquid phase separation, *Curr. Opin. Colloid Interface Sci.*, 2021, **53**, 101422, DOI: 10.1016/j.cocis.2021.101422.
24 E. Spruijt, J. Sprakel, M. A. Cohen Stuart and J. van der Gucht, Interfacial tension between a complex coacervate phase and its coexisting aqueous phase, *Soft Matter*, 2010, **6**(1), 172–178, DOI: 10.1039/B911541B.
25 Q. Huang and Z. Zhang, Evaluation of gum arabic and gelatine coacervated microcapsule morphology and core oil encapsulation efficiency by combining the spreading coefficient and two component surface energy theory, *Green Chem. Eng.*, 2025, **6**(3), 420–429, DOI: 10.1016/j.gce.2024.10.006.
26 E. Duhoranimana, J. Yu and O. Mukeshimana, *et al.*, Thermodynamic characterization of Gelatin–Sodium carboxymethyl cellulose complex coacervation encapsulating Conjugated Linoleic Acid (CLA), *Food Hydrocolloids*, 2018, **80**, 149–159, DOI: 10.1016/j.foodhyd.2018.02.011.

27 L. Li, B. Lai, J. N. Yan, M. H. Yambazi, C. Wang and H. T. Wu, Characterization of complex coacervation between chia seed gum and whey protein isolate: Effect of pH, protein/polysaccharide mass ratio and ionic strength, *Food Hydrocolloids*, 2024, **148**, 109445, DOI: 10.1016/j.foodhyd.2023.109445.

28 G. Q. Huang, J. X. Xiao, H. W. Qiu and J. Yang, Cross-linking of soybean protein isolate–chitosan coacervate with transglutaminase utilizing capsanthin as the model core, *J. Microencapsulation*, 2014, **31**(7), 708–715, DOI: 10.3109/02652048.2014.918665.

29 L. A. Bosnea, T. Moschakis and C. G. Biliaderis, Complex Coacervation as a Novel Microencapsulation Technique to Improve Viability of Probiotics Under Different Stresses, *Food Bioprocess Technol.*, 2014, **7**(10), 2767–2781, DOI: 10.1007/s11947-014-1317-7.

30 L. A. Bosnea, T. Moschakis, P. S. Nigam and C. G. Biliaderis, Growth adaptation of probiotics in biopolymer-based coacervate structures to enhance cell viability, *LWT*, 2017, **77**, 282–289, DOI: 10.1016/j.lwt.2016.11.056.

31 T. Moschakis and C. G. Biliaderis, Biopolymer-based coacervates: Structures, functionality and applications in food products, *Curr. Opin. Colloid Interface Sci.*, 2017, **28**, 96–109, DOI: 10.1016/j.cocis.2017.03.006.

32 A. N. Hassan, R. Ipsen, T. Janzen and K. B. Qvist, Microstructure and Rheology of Yogurt Made with Cultures Differing Only in Their Ability to Produce Exopolysaccharides, *J. Dairy Sci.*, 2003, **86**(5), 1632–1638, DOI: 10.3168/jds.S0022-0302(03)73748-5.

33 E. Çakır, C. J. Vinyard, G. Essick, C. R. Daubert, M. Drake and E. A. Foegeding, Interrelations among physical characteristics, sensory perception and oral processing of protein-based soft-solid structures, *Food Hydrocolloids*, 2012, **29**(1), 234–245, DOI: 10.1016/j.foodhyd.2012.02.006.

34 E. Çakır and E. A. Foegeding, Combining protein microphase separation and protein–polysaccharide segregative phase separation to produce gel structures, *Food Hydrocolloids*, 2011, **25**(6), 1538–1546, DOI: 10.1016/j.foodhyd.2011.02.002.

35 I. Vinterbladh, R. H. Soussi, J. Forsman, S. Bouhallab and M. Lund, Strong electrostatic attraction drives milk heteroprotein complex coacervation, *Int. J. Biol. Macromol.*, 2025, **286**, 137790, DOI: 10.1016/j.ijbiomac.2024.137790.

36 F. Niu, M. Kou and J. Fan, *et al.*, Structural characteristics and rheological properties of ovalbumin-gum arabic complex coacervates, *Food Chem.*, 2018, **260**, 1–6, DOI: 10.1016/j.foodchem.2018.03.141.

37 S. A. Faroughi and C. Huber, A generalized equation for rheology of emulsions and suspensions of deformable particles subjected to simple shear at low Reynolds number, *Rheol. Acta*, 2015, **54**(2), 85–108, DOI: 10.1007/s00397-014-0825-8.

38 S. Majumder, S. Coupe, N. Fakhri and A. Jain, Sequence-encoded intermolecular base pairing modulates fluidity in DNA and RNA condensates, *Nat. Commun.*, 2025, **16**, 4258, DOI: 10.1038/s41467-025-59456-0.

39 M. D. A. Rodriguez, D. C. Vidotto, A. A. O. Xavier, R. A. Mantovani and G. M. Tavares, Does the protein structure of β-lactoglobulin impact its complex coacervation with type A gelatin and the ability of the complexes to entrap lutein?, *Food Hydrocolloids*, 2023, **140**, 108651, DOI: 10.1016/j.foodhyd.2023.108651.

40 X. Wan, M. Zhao and M. Guo, *et al.*, Characterization of coacervation behavior between whey protein isolate and gum Arabic: Effects of heat treatment, *Food Chem.: X*, 2023, **18**, 100703, DOI: 10.1016/j.fochx.2023.100703.

41 X. Peng, Y. Li and T. Li, *et al.*, Coacervate-Derived Hydrogel with Effective Water Repulsion and Robust Underwater Bioadhesion Promotes Wound Healing, *Adv. Sci.*, 2022, **9**(31), 220890, DOI: 10.1002/advs.202203890.

42 M. Anvari, C. H. Pan, W. B. Yoon and D. Chung, Characterization of fish gelatin–gum arabic complex coacervates as influenced by phase separation temperature, *Int. J. Biol. Macromol.*, 2015, **79**, 894–902, DOI: 10.1016/j.ijbiomac.2015.06.004.

43 J. Ryu, X. Xiang and X. Hu, *et al.*, Assembly of plant-based meat analogs using soft matter physics: a coacervation-shearing-gelation approach, *Food Hydrocolloids*, 2023, **142**, 108817, DOI: 10.1016/j.foodhyd.2023.108817.

44 B. Hu, C. Zhang and J. Zhu, *et al.*, Liquid−liquid biopolymers aqueous solution segregative phase separation in food: from fundamentals to applications—A review, *Int. J. Biol. Macromol.*, 2024, **265**, 131044, DOI: 10.1016/j.ijbiomac.2024.131044.

45 B. M. Khan, K. L. Cheong and Y. Liu, ATPS: ''Aqueous two-phase system'' as the ''answer to protein separation'' for protein-processing food industry, *Crit. Rev. Food Sci. Nutr.*, 2019, **59**(19), 3165–3178, DOI: 10.1080/10408398.2018.1486283.

46 V. Y. Grinberg and V. B. Tolstoguzov, Thermodynamic incompatibility of proteins and polysaccharides in solutions, *Food Hydrocolloids*, 1997, **11**(2), 145–158, DOI: 10.1016/S0268-005X(97)80022-7.

47 V. Tolstoguzov, Compositions and Phase Diagrams for Aqueous Systems Based on Proteins and Polysaccharides, *Int. Rev. Cytol.*, 1999, **192**, 3–31, DOI: 10.1016/S0074-7696(08)60520-3.

48 C. G. de Kruif and R. Tuinier, Polysaccharide protein interactions, *Food Hydrocolloids*, 2001, **15**(4–6), 555–563, DOI: 10.1016/S0268-005X(01)00076-5.

49 S. Baldor, M. N. Enatarriaga-Scull, A. G. Genna-Coronel, P. B. Torres, C. F. Narambuena and V. Boeris, Segregative phase separation in aqueous systems of whey protein and carboxymethylcellulose under isoionic conditions, *Agrociencia Uruguay*, 2025, **29**(NE1), e1602, DOI: 10.31285/AGRO.29.1602.

50 A. Madadlou, A. Saint-Jalmes, F. Guyomarc'h, J. Floury and D. Dupont, Development of an aqueous two-phase emulsion using hydrophobized whey proteins and erythritol, *Food Hydrocolloids*, 2019, **93**, 351–360, DOI: 10.1016/j.foodhyd.2019.02.031.

51 E. B. A. Hinderink, A. Boire and D. Renard, *et al.*, Combining plant and dairy proteins in food colloid design, *Curr. Opin. Colloid Interface Sci.*, 2021, **56**, 101507, DOI: 10.1016/j.cocis.2021.101507.

52 T. Nicolai, Gelation of food protein-protein mixtures, *Adv. Colloid Interface Sci.*, 2019, **270**, 147–164, DOI: 10.1016/j.cis.2019.06.006.
53 S. M. Fitzsimons, D. M. Mulvihill and E. R. Morris, Segregative interactions between gelatin and polymerised whey protein, *Food Hydrocolloids*, 2008, **22**(3), 485–491, DOI: 10.1016/j.foodhyd.2007.01.005.
54 B. Zeeb, T. Jost, D. J. McClements and J. Weiss, Segregation Behavior of Polysaccharide–Polysaccharide Mixtures—A Feasibility Study, *Gels*, 2019, **5**(2), 26, DOI: 10.3390/gels5020026.
55 V. Tolstoguzov, Texturising by phase separation, *Biotechnol. Adv.*, 2006, **24**(6), 626–628, DOI: 10.1016/j.biotechadv.2006.07.001.
56 G. Ben Messaoud, E. Stefanopoulou, M. Wachendörfer, S. Aveic, H. Fischer and W. Richtering, Structuring gelatin methacryloyl – dextran hydrogels and microgels under shear, *Soft Matter*, 2024, **20**(4), 773–787, DOI: 10.1039/D3SM01365K.
57 B. L. Dekkers, R. Hamoen, R. M. Boom and A. J. van der Goot, Understanding fiber formation in a concentrated soy protein isolate – Pectin blend, *J. Food Eng.*, 2018, **222**, 84–92, DOI: 10.1016/j.jfoodeng.2017.11.014.
58 J. H. Chiang, S. M. Loveday, A. K. Hardacre and M. E. Parker, Effects of soy protein to wheat gluten ratio on the physicochemical properties of extruded meat analogues, *Food Struct.*, 2019, **19**, 100102, DOI: 10.1016/j.foostr.2018.11.002.
59 B. L. Dekkers, D. W. de Kort, K. J. Grabowska, B. Tian, H. Van As and A. J. van der Goot, A combined rheology and time domain NMR approach for determining water distributions in protein blends, *Food Hydrocolloids*, 2016, **60**, 525–532, DOI: 10.1016/j.foodhyd.2016.04.020.
60 B. L. Dekkers, M. A. Emin, R. M. Boom and A. J. van der Goot, The phase properties of soy protein and wheat gluten in a blend for fibrous structure formation, *Food Hydrocolloids*, 2018, **79**, 273–281, DOI: 10.1016/j.foodhyd.2017.12.033.
61 S. Guido, M. Simeone and A. Alfani, Interfacial tension of aqueous mixtures of Na-caseinate and Na-alginate by drop deformation in shear flow, *Carbohydr. Polym.*, 2002, **48**(2), 143–152, DOI: 10.1016/S0144-8617(01)00220-X.
62 K. F. Kapiamba, Mini-review of the microscale phenomena during emulsification of highly concentrated emulsions, *Colloid Interface Sci. Commun.*, 2022, **47**, 100597, DOI: 10.1016/j.colcom.2022.100597.
63 K. Verhulst, R. Cardinaels, P. Moldenaers, S. Afkhami and Y. Renardy, Influence of viscoelasticity on drop deformation and orientation in shear flow. Part 2: Dynamics, *J. Nonnewton Fluid Mech.*, 2009, **156**(1–2), 44–57, DOI: 10.1016/j.jnnfm.2008.10.003.
64 R. G. Larson, *The Structure and Rheology of Complex Fluids*, Oxford University Press, 1999.
65 V. Calabrese, S. Varchanis, S. J. Haward and A. Q. Shen, Alignment of Colloidal Rods in Crowded Environments, *Macromolecules*, 2022, **55**(13), 5610–5620, DOI: 10.1021/acs.macromol.2c00769.
66 H. Ramli, N. F. A. Zainal, M. Hess and C. H. Chan, Basic principle and good practices of rheology for polymers for teachers and beginners, *Chem. Teach. Int.*, 2022, **4**(4), 307–326, DOI: 10.1515/cti-2022-0010.
67 R. G. Ricarte and S. Shanbhag, A tutorial review of linear rheology for polymer chemists: basics and best practices for covalent adaptable networks, *Polym. Chem.*, 2024, **15**(9), 815–846, DOI: 10.1039/D3PY01367G.
68 S. Narayan, D. B. Moravec, A. J. Dallas and C. S. Dutcher, Droplet shape relaxation in a four-channel microfluidic hydrodynamic trap, *Phys. Rev. Fluids*, 2020, **5**(11), 113603, DOI: 10.1103/PhysRevFluids.5.113603.
69 E. Atefi, J. A. Mann and H. Tavana, Ultralow Interfacial Tensions of Aqueous Two-Phase Systems Measured Using Drop Shape, *Langmuir*, 2014, **30**(32), 9691–9699, DOI: 10.1021/la500930x.
70 F. Spyropoulos, W. J. Frith, I. T. Norton, B. Wolf and A. W. Pacek, Sheared aqueous two-phase biopolymer–surfactant mixtures, *Food Hydrocolloids*, 2008, **22**(1), 121–129, DOI: 10.1016/j.foodhyd.2007.04.016.
71 W. J. Frith, Mixed biopolymer aqueous solutions – phase behaviour and rheology, *Adv. Colloid Interface Sci.*, 2010, **161**(1–2), 48–60, DOI: 10.1016/j.cis.2009.08.001.
72 H. A. Stone, Dynamics of Drop Deformation and Breakup in Viscous Fluids, *Annu. Rev. Fluid Mech.*, 1994, **26**(1), 65–102, DOI: 10.1146/annurev.fl.26.010194.000433.
73 J. M. Rallison, The Deformation of Small Viscous Drops and Bubbles in Shear Flows, *Annu. Rev. Fluid Mech.*, 1984, **16**(1), 45–66, DOI: 10.1146/annurev.fl.16.010184.000401.
74 P. L. Maffettone and M. Minale, Equation of change for ellipsoidal drops in viscous flow, *J. Nonnewton Fluid Mech.*, 1998, **78**(2–3), 227–241, DOI: 10.1016/S0377-0257(98)00065-2.
75 A. R. Bunsell, S. Joannès and A. Marcellan, Testing and characterization of fibers, *Handbook of Properties of Textile and Technical Fibres*, Elsevier, 2018, pp. 21–55, DOI: 10.1016/B978-0-08-101272-7.00002-X.
76 Z. Xu, H. Chen and H. B. Yang, *et al.*, Hierarchically aligned heterogeneous core-sheath hydrogels, *Nat. Commun.*, 2025, **16**(1), 400, DOI: 10.1038/s41467-024-55677-x.
77 L. M. Dedroog, O. Deschaume and C. J. G. Abrego, *et al.*, Stress-controlled shear flow alignment of collagen type I hydrogel systems, *Acta Biomater.*, 2022, **150**, 128–137, DOI: 10.1016/j.actbio.2022.07.008.